Sangodoyin, S.; Virk, U. T.; Burghal, D.; Haneda, K.; Molisch, A. F.

Joint Characterization of MM-Wave and CM-Wave Device-to-Device Fading Channels

Published in:
2018 IEEE Military Communications Conference, MILCOM 2018

DOI:
10.1109/MILCOM.2018.8599827

Published: 01/01/2018

Document Version
Peer-reviewed accepted author manuscript, also known as Final accepted manuscript or Post-print

Please cite the original version:
Sangodoyin, S., Virk, U. T., Burghal, D., Haneda, K., & Molisch, A. F. (2018). Joint Characterization of MM-Wave and CM-Wave Device-to-Device Fading Channels. In *2018 IEEE Military Communications Conference, MILCOM 2018* (Vol. 2019-October, pp. 194-200). Article 8599827 (IEEE Military Communications Conference proceedings). IEEE. https://doi.org/10.1109/MILCOM.2018.8599827

Joint Characterization of mm-wave and cm-wave Device-to-Device Fading Channels

S. Sangodoyin[1], *Member, IEEE*, U. T. Virk[2], D. Burghal[1], *Student Member, IEEE*, K. Haneda[2] *Member, IEEE,* and A. F. Molisch[1], *Fellow, IEEE*,

[1] University of Southern California, Los Angeles, CA USA.
[2] Aalto University, Espoo, Finland.
Email: [1]{sangodoy, burghal, molisch}@usc.edu; [2]{usman.virk, katsuyuki.haneda}@aalto.fi

***Abstract*—Device-to-Device (D2D) wireless communications has many envisioned applications such as proximity-based networking, tactical communications and situation awareness of military personnel in a battlefield. The joint use of multiple frequency bands could provide further enhancement to existing D2D wireless system and localization architectures. However, the development of any suitable communication system with this capability will requires accurate propagation channel measurement and modeling to understand channel frequency dependencies in an environment in which the system will operate. In this paper, we present a detailed description of a propagation channel measurement campaign performed in an outdoor environment within the millimeter wave (mm-wave) $59-63$ GHz and centimeter wave (cm-wave) $2-6$ GHz frequency bands. The measurements were conducted for both line-of-sight (LOS) and non-line-of-sight (NLOS) scenarios. We extracted (and compared) propagation channel parameters such as distance-dependent pathloss exponent (γ), shadowing gain (ξ_σ), root-mean-square (rms) delay spread (τ_{rms}) and amplitude fading statistics to motivate a suitable channel model in both bands. The model developed can be used for realistic performance evaluations of devices operating in the cm-wave and/or mm-wave bands.**

I. Introduction

Device-to-Device (D2D) communications in which information is exchanged via a direct link between nodes or sensors without interfacing with the infrastructure, such as cell towers, available in traditional cellular networks, serves as a possible solution to overcome the limitations of existing infrastructure-based wireless communication. The Third Generation Partnership Project (3GPP) is actively pursuing the standardization of D2D communication [1]. D2D wireless systems have already been deployed for use in different applications such as wireless sensor networks and broadband communications in battlefields [2], [3], as well as in the localization of rescue workers in emergency or disaster relief zones [4].

The centimeter wave (cm-wave) and millimeter wave (mm-wave) bands have been proposed as complimentary frequency bands to be used for next-generation communication systems. The cm-wave band offers several advantages, which include; better coverage due to smaller pathloss and ability to penetrate walls, while the mm-wave band affords higher data-rates due to large spectrum availability and less interference. Electromagnetic (EM) wave propagation in these two frequency bands differs greatly. Unlike cm-wave, mm-wave frequencies have increased reflectivity and scattering from common objects (e.g. walls or human body), poor diffraction and penetration capabilities. These properties of the mm-wave make the environment dependent characteristics more pronounced and are probably the main factor distinguishing them from the characteristics at lower frequencies.

Accurate channel characteristics are required for the development of any wireless communication systems, hence it is of utmost importance that the channel in which the wireless system is to be deployed be duly investigated through propagation channel measurements.

A number of works [5]–[10] in the literature have sought to compare propagation in different frequency bands by conducting channel measurements. Note that these measurements were conducted for *non-cellular* related scenarios. Directional channel measurements were conducted by [5] at $5.8, 14.8$ and 58.7 GHz while [6] conducted similar measurements at $2, 15, 28$ and 60 GHz. However, these measurements were conducted in an indoor environment. [7] conducted measurements at 15 and 28 GHz in an urban street environment, while [8] and [9] conducted measurements at $15, 28$ and 60 GHz bands in airport and street canyon respectively. A wide range of frequencies ($2-86$ GHz) were measured in [10], however, the only result presented was the delay spread. Works comparing the propagation characteristics of cm-wave and mm-wave frequency bands in outdoor environments are scarce in the literature.

In this paper, we remedy this by investigating and jointly characterizing propagation in the cm-wave and mm-wave bands. We present details of a dual-band propagation channel measurement campaign performed in an outdoor environment. We explored various scenarios such as Line-of-sight (LOS) and Non-line-of-sight (NLOS) cases. We quantify and compare results for key channel parameters such as the as distance-dependent pathloss (γ), shadowing gain (ξ_σ), root-mean-square (rms) delay spread (τ_{rms}) and amplitude fading statistics of multipath components (MPCs) in both bands.

The rest of the paper is organized as follows. Section II describes the measurement environment. Section III describes the measurement setup. Data processing procedure and results are discussed in Section IV while conclusions are inferred in Section V.

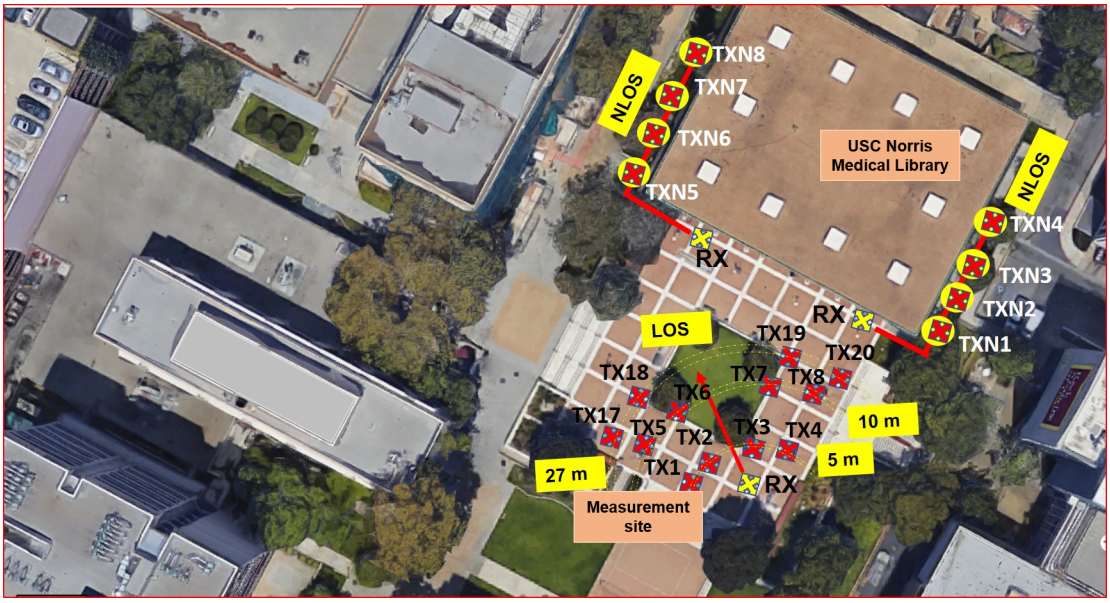

Fig. 1: Measurement points at the quad

II. Measurement Environment

Measurements were performed at a quadrangle (quad) located in front of the Norris Medical Library on the Health science campus (HSC) of the University of Southern California (USC) in Los Angeles, CA, USA. The quad and the measurement locations are shown in Fig.1. The quad is a 33 $\times$ 33 m open square surrounded by buildings and trees. At the center of the quad is a 15 $\times$ 15 m demarcation, where trees and flowers are planted. The ground of the quad is paved with brick slabs with lamp-posts placed alongside its edges. Buildings surrounding the measurement location (such as the Norris medical library) are made up of a mixture of concrete, steel bar railing and glass window pane.

Measurements were conducted for LOS and NLOS scenarios in and around the quad at TX-RX separation distances of $5, 10, 15, 24$ and 27 m respectively. Multiple measurements were taken for each distance measured, by placing the TX and RX array at different positions. These positions provide different realizations of shadowing i.e., power-variations due to blockage effects in the environment. A total of four shadowing positions were selected at each distance measured therefore 80 positions[1] were measured in our campaign. The exact same locations (with constituents unchanged) were measured with both cm-wave and mm-wave bands for comparability of results.

III. Measurement Setup

A dual-band channel sounder system, which uses an 8×8 virtual MIMO antenna array configuration was assembled for our measurement campaign. This sounder operates in both cm-wave ($2-6$ GHz) and mm-wave ($59-63$ GHz) frequency range. The channel sounder was designed to be backwards compatible, i.e., only a small number of components needed to be replaced to go from a cm-wave to a mm-wave setup. A description of the sounder configuration in each band is discussed subsequently, while extensive details are provided in [11].

A. cm-wave

At the heart of the cm-wave channel sounder setup (see Fig. 2) is a vector network analyzer (VNA, KT-N5222A-200/WXP), which was used for obtaining the complex transfer function of the radio channel[2]. The VNA in combination with a coaxial cables, an electro-optical (with fiber-optics cable connection) converter modules, a power amplifier (rated at 37 dB gain) and two omni-directional biconical antennas (TX and RX), a 33 dB low noise amplifier was used to transmit and receiver signals. A stepped frequency sweep was conducted over 5001 points within the $2-6$ GHz band on the VNA. Parameter setting for the VNA are shown in Table I.

The *virtual* MIMO antenna array configuration used at both TX and RX ends was implemented by attaching an omni-direction biconical antenna to a 1.54-m-high support pole, which was in turn fastened to a stepper motor steered linear positioner controlled by LabView software. The biconical antenna was moved to different positions by the linear positioner, thus creating a *virtual* uniform linear array (ULA). The separation between antenna elements is 50 mm; hence by moving each antenna over a distance of 400 mm at both ends, eight antenna positions at each link end are measured, providing a total of 64 spatial sub-channels. Due to array positioner movement time and VNA frequency sweep time

[1]Note that the 80 points = 5 separations $\times$ 4 shadowing $\times$ 2 scenarios (LOS and NLOS) $\times$ 2 bands (cm-wave and mm-wave bands).

[2]Note that the radio channel implies the combination of TX and RX antennas and the propagation channel.

(over a 4 GHz bandwidth), the total measurement time for each position was 48 minutes.

B. mm-wave

In the mm-wave measurements setup (see Fig. 3), the radio frequency (RF) signal transmission and reception was realized by using the cm-wave setup in conjunction with up- and down-converters modules. The up- and down-converter modules were used for mixing a 4 GHz bandwidth intermediate frequency (IF) signal from the VNA with a (TX-RX synchronized) local oscillator (LO) signal generated by a frequency synthesizer. Optical fiber cables (via electro-optical converters) were used in transporting the IF and LO signals from the VNA and the frequency synthesizer to the up-converter module while a 7.62 m coaxial cable was used at the RX side to transport the down-converted received signal (from a 60 GHz biconical antenna) back to the VNA on the RX side.

Similarly to the cm-wave sounder configuration, a *virtual* MIMO antenna setup was used here as well, however, a 2.5 mm separation between antenna elements was used instead, therefore by moving each antenna over a distance of 20 mm at both ends, eight antenna positions at each link end were realized thereby providing a total of 64 spatial sub-channels. The total measurement time in this case was 22 minutes for each position measured.

cm-wave parameters	
Parameter	**Setting**
Bandwith	4 GHz ($2-6$ GHz)
Transmitted Power	10 dBm
Center frequency f_c	4 GHz
Number of spatial sub-channels	64
Number of sub-carriers	5001
mm-wave parameters	
Parameter	**Setting**
Bandwith	4 GHz ($59-63$ GHz)
Transmitted Power	16 dBm
Center frequency f_c	61 GHz
Number of spatial sub-channels	64
Number of sub-carriers	5001

TABLE I: Channel Measurement parameters

IV. Data Processing and Results

The channel transfer function was extracted from the data captured from the VNA after each measurement run. To facilitate our discussion in this work, the transfer function will be denoted as $H_{d,S_d,m_{\mathrm{R}},m_{\mathrm{T}},f_k}$, where $m_{\mathrm{T}} = 1,...,M_{\mathrm{T}} = 8$ and $m_{\mathrm{R}} = 1,...,M_{\mathrm{R}} = 8$ denote the TX and RX antenna positions in the MIMO array, $f_k = 1,...,M_f = 5001$ represents the frequency indexes, $d = 1,...,D = 5$ represents the TX-RX (separation) distances measured, and shadowing locations are represented by $S_d = 1,...,M_{S_d} = 4$. The measured $H_{d,S_d,m_{\mathrm{R}},m_{\mathrm{T}},f_k}$ was transformed to the delay domain

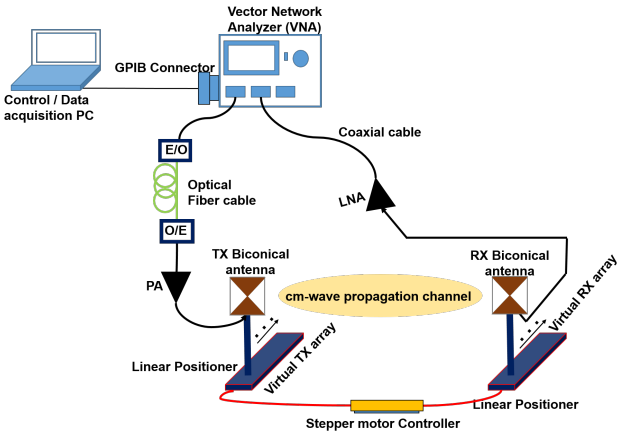

Fig. 2: cm-wave channel sounder setup.

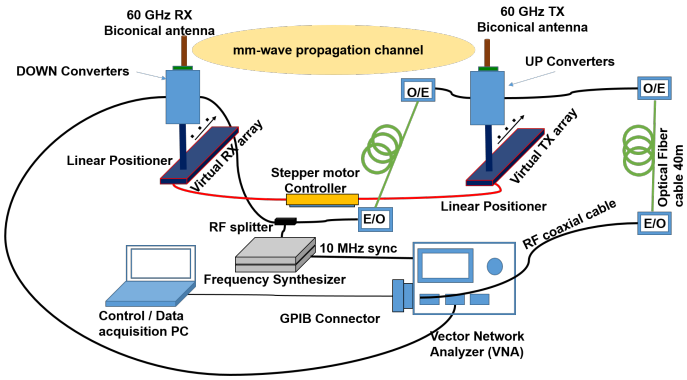

Fig. 3: mm-wave channel sounder setup.

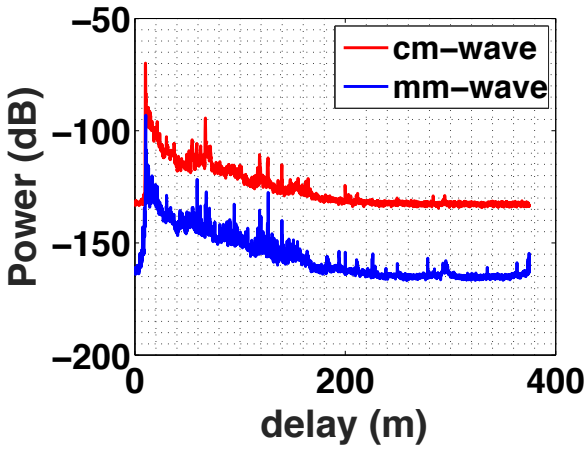

Fig. 4: Sample plots of APDP from 10 m LOS scenario from measurement at both cm-wave and mm-wave bands

by using an inverse Fourier transform; the resulting impulse response is denoted as $h_{d,S_d,m_{\mathrm{R}},m_{\mathrm{T}},\tau_k}$; a Hann instantaneous window was applied to suppress temporal side lobes.

From the impulse response, the power-delay-profile (PDP), i.e., $P_{d,S_d,m_{\mathrm{R}},m_{\mathrm{T}},\tau_k} = |h_{d,S_d,m_{\mathrm{R}},m_{\mathrm{T}},\tau_k}|^2$ can be obtained. For each shadowing location, the influence of small-scale fading

is removed by averaging the instantaneous PDPs over the 8×8 TX/RX positions to obtain the average-power-delay-profile (APDP, $\hat{P}_{d,S_d,\tau_k}$).

$$\hat{P}_{d,S_d,\tau_k} = \frac{1}{M_{\mathrm{T}} \cdot M_{\mathrm{R}}} \sum_{m_{\mathrm{T}}}^{M_{\mathrm{T}}} \sum_{m_{\mathrm{R}}}^{M_{\mathrm{R}}} P_{d,S_d,m_{\mathrm{R}},m_{\mathrm{T}},\tau_k} \quad (1)$$

A sample of the averaged power-delay profile (APDP) ($\hat{P}_{d,S_d,\tau_k}$) plot at a select distance for both cm-wave and mm-wave LOS measurements is shown in Fig. 4. A noise thresholding filter was implemented such that all APDP samples whose magnitude are below a certain threshold are set to zero. The chosen threshold value used in this work was 6 dB above the noise floor of the APDP as done in [12]. We recognize that the use of 6 dB noise level could lead to reduced dynamic range in the mm-wave than cm-wave measurements, thereby affecting the received power computation. To investigate the impact of this, we analyzed the data with two alternative approaches: (i) using a fixed dynamic range (30 dB from peak) for both bands, and (ii) enforcing the smallest (among all measurements) available dynamic range for all measurements. While not shown here for space reasons, the relative comparisons between cm- and mm-wave bands do not show significant differences. More details will be reported in [11].

A. *Pathloss Modeling*

The distance-dependent pathloss is derived from the noise-filtered APDP by summing up all powers of delay bins. The APDPs are obtained from measurements at different locations. The distance-dependent pathloss can be modeled by using the conventional power-law equation (see (2)),

$$G_d(\mathrm{dB}) = G_{d_0} + 10 \cdot \gamma \cdot \log_{10}\left(\frac{d}{d_0}\right) + \xi_\sigma(\mathrm{dB}), \quad (2)$$

where γ is the pathloss exponent, d_0 is the reference distance, G_{d_0} is the pathloss at the reference distance (1 m) and ξ_σ is the shadowing gain. Figs. 5 and 6 show scatter plot and linear regression fit of the pathloss for all measurements conducted at different distances at cm-wave and mm-wave bands for LOS and NLOS scenarios, while all extracted pathloss model parameters are available in Table II.

	LOS		NLOS	
Scenario	γ	G_{d_0} (dB)	γ	G_{d_0} (dB)
cm-wave	-1.75	-45.21	-2.51	-55.35
mm-wave	-1.91	-71.97	-2.37	-84.87

TABLE II: Pathloss model parameters for cm-wave and mm-wave bands.

It can be observed from Table II that there differences between the parameters extracted at the two different bands as there is a higher pathloss in mm-wave band measurements when compared to cm-wave band in both LOS and NLOS scenarios. These results are in alignment with numerous observations in the literature that electromagnetic waves are more susceptible to attenuation at higher frequencies.

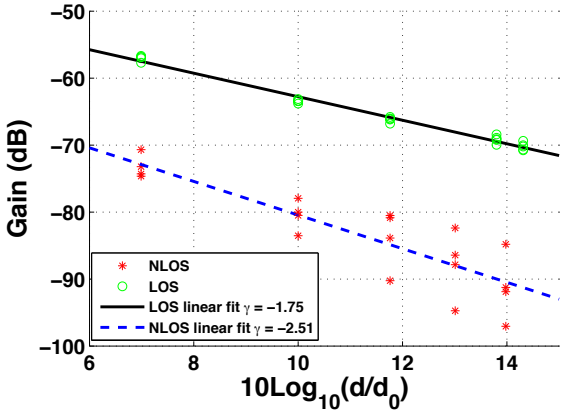

Fig. 5: Scatterplot of pathloss and linear regression fit for all measurements at cm-wave band.

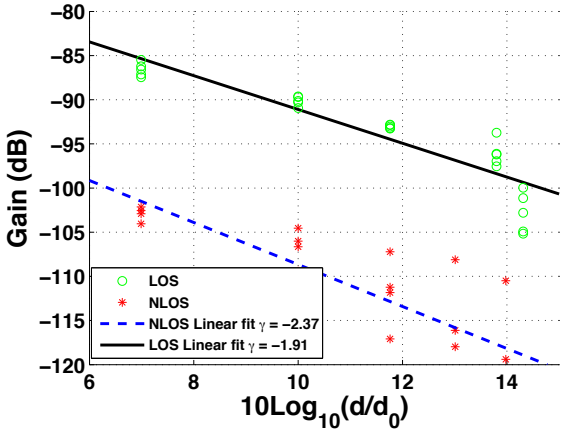

Fig. 6: Scatterplot of pathloss and linear regression fit for all measurements at mm-wave band.

B. *Shadowing Gain Modeling*

The shadowing gain (denoted ξ_σ in (2)) accounts for the large-scale fluctuations of the received power at each measured distance. We have modeled the logarithmic equivalent of the shadowing gain as a zero-mean Gaussian distribution $N(0, \sigma(\mathrm{dB}))$ in our work. The standard deviation (std. dev) values for the shadowing gain from our measurements is provided in Table III while plots showing the empirical distribution of the shadowing gain and the corresponding Gaussian distribution fit used for modeling the shadowing gain at both cm-wave and mm-wave bands are provided in Figs. 7 and 8.

From Table III, it can be observed that shadowing is more pronounced in the mm-wave band than in the cm-wave band for both LOS and NLOS scenarios.

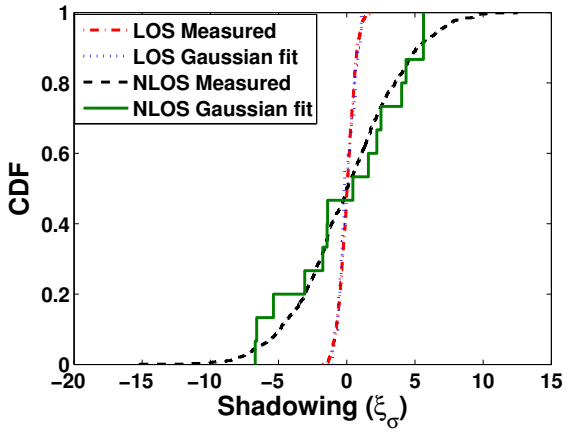

Fig. 7: CDF of Shadowing gain at cm-wave band.

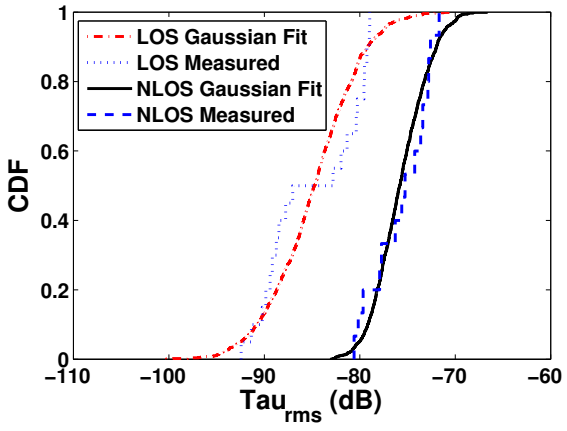

Fig. 9: CDF of $\tau_{\mathrm{rms}}(\mathrm{dBs})$ at cm-wave band.

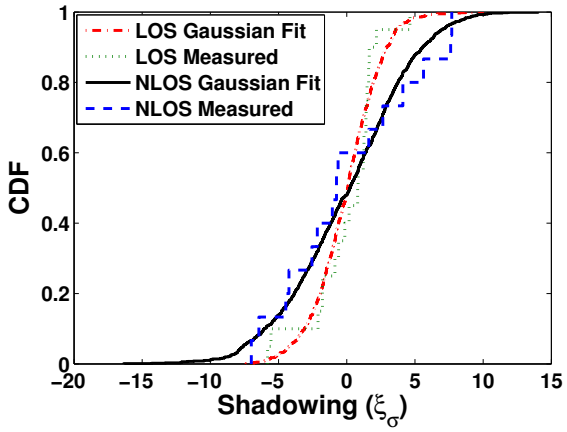

Fig. 8: CDF of Shadowing gain at mm-wave band.

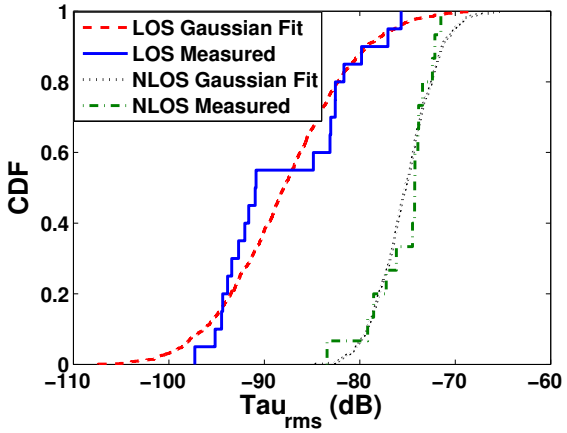

Fig. 10: CDF of $\tau_{\mathrm{rms}}(\mathrm{dBs})$ at mm-wave band.

	LOS	NLOS
Scenario	**std. dev (σ (dB))**	**std. dev (σ (dB))**
cm-wave	0.61	3.47
mm-wave	2.43	4.11

TABLE III: Shadowing gain parameters for cm-wave and mm-wave modeling

C. Delay Dispersion Statistics

The rms delay spread (τ_{rms}) serves to compactly describe the effects of delay dispersion in multi path environments. In this work, the rms delay spread values have been modeled to follow a lognormal distribution $N(\mu_\tau(\mathrm{dB}), \sigma_\tau(\mathrm{dB}))$. Estimated values for $\mu_\tau(\mathrm{dB})$ and $\sigma_\tau(\mathrm{dB})$ are provided in Table IV, while plots showing statistical distribution fit for the logarithmic equivalent for τ_{rms} are provided Figs. 9 and 10.

From the values in Table IV, we can deduce that there is less dispersion in mm-wave propagation when compared to cm-wave in LOS, while dispersion in NLOS seems fairly similar.

According to [13], the rms delay-spread increases with the distance between the TX and RX. Assuming that this dependency can be modeled using (3), the decay exponent ϵ can be extracted to give information about the relationship between the τ_{rms} and distance for each band and scenario measured.

$$\tau_{\mathrm{rms}}(\mathrm{dB}) = G_{\mathrm{T}_0}(\mathrm{dB}) + 10 \cdot \epsilon \cdot \log_{10}\left(\frac{d}{d_0}\right) + L_{\sigma_{\mathrm{T}}}. \quad (3)$$

In (3), d is the distance between TX and RX, G_{T_0} the intercept of the ordinate, ϵ the slope parameter and $L_{\sigma_{\mathrm{T}}}$ a normally distributed random variable i.e., $N(0, \sigma_{L_{\sigma_{\mathrm{T}}}}(\mathrm{dB}))$.

A linear regression fit was used in estimating all parameters from a scatterplot as shown in Figs. 11 and 12 in cm-wave and mm-wave bands respectively. The aforementioned parameters are listed in Table IV.

From Table IV exponents (ϵ) are positive as expected, which implies that the τ_{rms} increases with distance irrespective of the frequency band or scenario, however the values of the modeling parameters differ according to the bands and scenarios measured.

	LOS		NLOS	
Scenario	μ_τ(dBs)	σ_τ(dBs)	μ_τ(dBs)	σ_τ(dBs)
cm-wave	-84.86	4.78	-75.62	2.86
mm-wave	-87.85	6.51	-75.26	3.06

	LOS			NLOS		
Parameters	ϵ	G_{T_0} (dBs)	$\sigma_{L_{\sigma_T}}$ (dB)	ϵ	G_{T_0} (dBs)	$\sigma_{\mathrm{L}_{\sigma_\mathrm{T}}}$ (dB)
cm-wave	1.35	-101.26	3.20	0.31	-79.10	2.85
mm-wave	1.72	-107.44	4.71	0.33	-79.00	3.05

TABLE IV: Parameters for τ_{rms} distribution for cm-wave and mm-wave channels

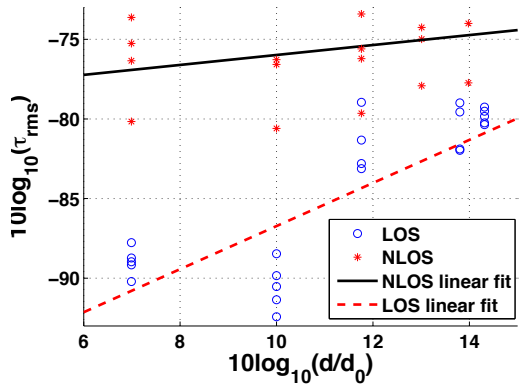

Fig. 11: τ_{rms}(dBs) as function of distance at cm-wave band.

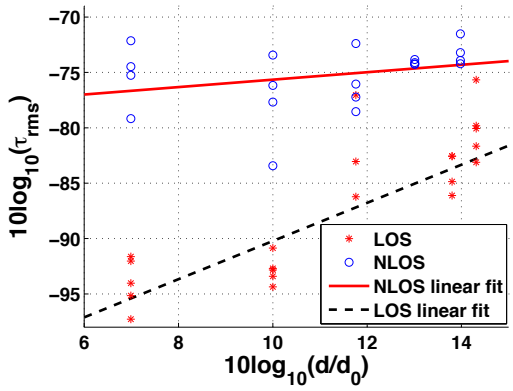

Fig. 12: τ_{rms}(dBs) as a function of distance at mm-wave band.

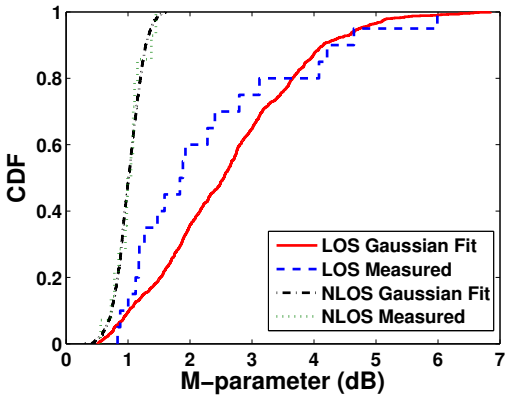

Fig. 13: CDF of $m-$parameter(dB) at cm-wave band.

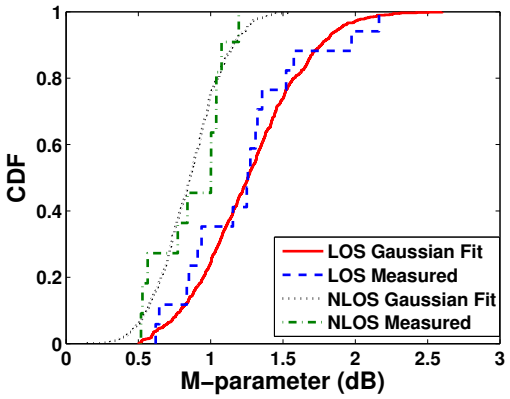

Fig. 14: CDF of $m-$parameter(dB) at mm-wave band.

D. Fading Statistics

Small-scale fading (SSF) in the propagation channel stems from multipath component interaction with local scatterers, which exist within the vicinity of the transmitter and receiver. For the cm-wave and mm-wave propagation, the SSF statistics was modeled as m-Nakagami distributed variables. This was investigated by considering fading over MIMO (spatial) sub-channels.

The m-parameter of the Nakagami distribution is itself a random variable (over an ensemble of measured locations) and was modeled using a lognormal distribution ($N(\mu_{\mathrm{m}}(\mathrm{dB}), \sigma_{\mathrm{m}}(\mathrm{dB}))$) at each band and scenario measured. Values for $\mu_{\mathrm{m}}(\mathrm{dB})$ and $\sigma_{\mathrm{m}}(\mathrm{dB})$ are provided in Table V while a statistical distribution fit for the logarithmic equivalent of the m-parameter is provided in Figs. 13 and 14.

From the results in Table V, the smaller statistical values of the m-parameter in the mm-wave band indicates a slightly wider range of signal envelope fluctuation in this band than the cm-wave band for the LOS scenario while the almost similar fading is experienced in both the cm-wave and mm-wave for the NLOS scenario.

	LOS		NLOS	
scenario	$\mu_m(\mathrm{dB})$	$\sigma_m(\mathrm{dB})$	$\mu_m(\mathrm{dB})$	$\sigma_m(\mathrm{dB})$
cm-wave	2.28	1.40	1.04	0.22
mm-wave	1.23	0.41	0.87	0.23

TABLE V: m-parameters for cm-wave and mm-wave.

V. Summary and Conclusion

We conducted a measurement campaign in an outdoor environment using a frequency domain channel sounder setup in both cm-wave and mm-wave bands. We found (omni-directional) channel parameters such as distance-dependent pathloss exponent (γ) to be similar in both cm-wave and mm-wave bands with values 1.75 and 1.91 for the LOS scenario while 2.51 and 2.37 in the NLOS case. However, the pathloss values at the reference distance was significantly larger by 26-29 dB in the mm-wave band than in the cm-wave band. We also found shadowing gain to be lognormal distributed with std. dev values larger (≈ 1.7 dB for LOS and ≈ 0.64 dB in NLOS) in the mm-wave band than cm-wave band. The rms-delay spread was modeled as a lognormal distribution. The statistical values of the τ_{rms} showed that the mm-wave channel exhibited less dispersion in delay as compared to the cm-wave channel in the LOS case. τ_{rms} also exhibited a linear increase for a longer TX-RX distance with all modeling parameters provided in Table IV. The small-scale fading statistic was modeled using an m-Nakagami distribution in both bands. The m-parameter turned out to be a random variable and as such was modeled as a Gaussian distribution. The mean values of the m-parameter were smaller in the mm-wave than cm-wave band thereby indicating that a wider range of signal envelope fluctuation due to small-scale fading is experienced in the mm-wave band in both LOS and NLOS scenarios.

Overall, we can observe that there is a difference between propagation channel parameters in the cm-wave and mm-wave bands for this type of environment. Details such as those provided in this work will be of great help for D2D systems design and simulation in this type of environment.

VI. Acknowledgment

This work was financially supported by a National Science Foundation WiFiUS grant 1457340.

References

[1] X. Lin, J. G. Andrews, A. Ghosh, and R. Ratasuk, "An overview of 3GPP device-to-device proximity services," *IEEE Communications Magazine*, vol. 52, no. 4, pp. 40–48, April 2014.

[2] S. Kolenchery, J. Townsend, and J. Freebersyser, "A novel impulse radio network for tactical military wireless communications," in *Military Communications Conference, 1998. MILCOM 98. Proceedings., IEEE*, vol. 1, Oct 1998, pp. 59–65 vol.1.

[3] S. Sangodoyin, S. Niranjayan, and A. F. Molisch, "A measurement-based model for outdoor near-ground ultrawideband channels," *IEEE Transactions on Antennas and Propagation*, vol. 64, no. 2, pp. 740–751, Feb 2016.

[4] A. Lo, L. Xia, I. Niemegeers, T. Bauge, M. Russell, and D. Harmer, "EUROPCOM - An Ultra-WideBand (UWB)-Based Ad Hoc Network for Emergency Applications," in *Vehicular Technology Conference, 2008. VTC Spring 2008. IEEE*, May 2008, pp. 6–10.

[5] J. Medbo, N. Seifi, and H. Asplund, "Frequency dependency of measured highly resolved directional propagation channel characteristics," in *European Wireless 2016; 22th European Wireless Conference*, May 2016, pp. 1–6.

[6] U. T. Virk, S. L. H. Nguyen, and K. Haneda, "Multi-frequency power angular spectrum comparison for an indoor environment," in *Proc. 2017 11th European Conference on Antennas and Propagation (EUCAP)*, March 2017, pp. 3389–3393.

[7] S. L. H. Nguyen and K. Haneda and J. Putkonen, "Dual-Band Multipath Cluster Analysis of Small-Cell Backhaul Channels in an Urban Street Environment," in *2016 IEEE Globecom Workshops (GC Wkshps)*, Dec 2016, pp. 1–6.

[8] J. Vehmas and J. Jarvelainen and S. L. H. Nguyen and R. Naderpour and K. Haneda, "Millimeter-Wave Channel Characterization at Helsinki Airport in the 15, 28, and 60 GHz Bands," in *2016 IEEE 84th Vehicular Technology Conference (VTC-Fall)*, Sept 2016, pp. 1–5.

[9] R. Naderpour and J. Vehmas and S. Nguyen and J. Jrvelinen and K. Haneda, "Spatio-temporal channel sounding in a street canyon at 15, 28 and 60 GHz," in *Proc. 2016 IEEE 27th Annual International Symposium on Personal, Indoor, and Mobile Radio Communications (PIMRC '16)*, Sept 2016, pp. 1–6.

[10] S. L. H. Nguyen, J. Medbo, M. Peter, A. Karttunen, K. Haneda, A. Bamba, R. D'Errico, N. Iqbal, C. Diakhate, and J. Conrat, "On the Frequency Dependency of Radio Channel's Delay Spread: Analyses and Findings From mmMAGIC Multi-frequency Channel Sounding," in *2018 12th European Conference on Antennas and Propagation (EUCAP)*, April 2018, pp. 1–5.

[11] S. Sangodoyin, U. Virk, D. Burghal, S. L. H. Nguyen, A. Karttunen, K. Haneda, and A. F. Molisch, "Mm-wave and cm-wave Device-to-Device MIMO Channel Characterization and Performance Evaluation for 5G Systems," *to be submitted*.

[12] S. Sangodoyin, V. Kristem, A. F. Molisch, R. He, F. Tufvesson, and H. M. Behairy, "Statistical Modeling of Ultrawideband MIMO Propagation Channel in a Warehouse Environment," *IEEE Transactions on Antennas and Propagation*, vol. 64, no. 9, pp. 4049–4063, Sept 2016.

[13] L. J. Greenstein, V.Erceg, Y. Shuan, and M. Clark, "A new path-gain/delay-spread propagation model for digital cellular channels," *IEEE Trans. Vehicular Techn.*, vol. 46, pp. 477–485, May 1997.